GEOPHYSICS, VOL. 78, NO. 4 (JULY-AUGUST 2013); P. E213–E223, 11 FIGS., 3 TABLES.
10.1190/GEO2012-0445.1

Background resistivity model from seismic velocities

Dieter Werthmüller[1], Anton Ziolkowski[1], and David Wright[1]

ABSTRACT

We developed a methodology to estimate resistivities from seismic velocities. We applied known methods, including rock physics, depth trends, structural information, and uncertainty analysis. The result is the range of background resistivity models that is consistent with the known seismic velocities. We successfully tested the methodology with real data from the North Sea. These 2D or 3D background resistivity models yield a detailed insight into the background resistivity, and they are a powerful tool for feasibility studies. They could also serve as starting models or constraints in (iterative) forward modeling of electromagnetic data for the determination of subsurface resistivities.

INTRODUCTION

Seismic and electromagnetic (EM) data yield complementary information about the subsurface. Seismic data yield a velocity model of the underlying structure. EM data provide insight into how the formations behave if an electric current is applied, which can be used to determine whether the pore fluids are conductive, for instance, brine, or resistive, for instance, hydrocarbons. Geophysicists process seismic data to get seismic velocities. Seismic velocities are derived from the data: they are the result of aligning seismic arrivals. This process of deriving a geophysical property directly from the data is not available to controlled-source EM (CSEM) data, as Ziolkowski and Wright (2012) discuss. There is no theory for the direct extraction of resistivities from CSEM data. Instead, resistivities are determined using the process of iterative forward modeling, which is often termed "inversion." In this process, synthetic data are generated from an initial model (a guess) of the subsurface resistivities, often a uniform half-space. The misfit between the synthetic and the measured data is minimized by adjusting this starting model. A range of schemes exists for how the model should be varied; Occam's razor of the simplest solution that matches the data is often applied in EM (Constable et al., 1987). We do not alter the measured EM data in this process, only the model. That is, the resistivities are derived from modeling, and they are not derived directly from the data.

It is therefore desirable to consult seismic velocities, if available, to gain a better understanding of the subsurface resistivities. However, getting from velocities to resistivities is not a trivial task because the underlying theories of seismic wave propagation and EM wave propagation share no physical property; see Table 1 and Ziolkowski and Engelmark (2009). The theory of seismic surveying is based on the wave equation and with it Hooke's law and Newton's second law of mechanics. These depend on the density and the elastic moduli of the rock, which define the P-wave and S-wave velocities. The theory of EM surveying, on the other hand, is based on Maxwell's equations, which depend on the magnetic permeability, electrical resistivity, and electrical permittivity of the rock. Unlike gravity data and seismic data, EM data and seismic data share no common parameter.

The most obvious way to combine these two data is to extract the structures from the interpreted seismic data and use them in (iterative) EM forward modeling (e.g., Harris et al., 2009). Another structural constraint is the cross-gradient method (e.g., Gallardo and Meju, 2007; Hu et al., 2009), in which it is assumed that the resistivity changes if the velocity changes. A different approach is to replace the missing link with rock physics, usually, but not always, via porosity. Carcione et al. (2007) present a nice overview of common relations. Engelmark (2010) emphasizes the importance of background (shale) modeling for EM inversions and the depth dependence of rock physics models.

Whatever the approach, the biggest problem remains: There is no physical link between velocity and resistivity. A change in velocity does not necessarily mean that there is a change in resistivity. That means that any of these methods can introduce unwanted bias. Chen and Dickens (2009) look at the effects of uncertainty involved in the rock physics model itself (intrinsic) and their parameters (extrinsic), and Myoung and Snieder (2011) show that the uncertainty of the

Manuscript received by the Editor 23 October 2012; revised manuscript received 5 February 2013; published online 26 June 2013.
[1]University of Edinburgh, School of GeoSciences, Grant Institute, Edinburgh, Scotland. E-mail: dieter.werthmuller@ed.ac.uk; anton.ziolkowski@ed.ac.uk; dwright3@staffmail.ed.ac.uk.

rock physics model contributes more to the overall uncertainty than the uncertainty in the data themselves.

The purpose of this work is to determine the range of resistivity models that is consistent with known seismic velocities. This is not fundamentally new: Constable and Srnka (2007), for instance, present a 3D resistivity model that was "guided by 3D seismic data, well-log data (. . .), and the CSEM data" but without explaining this guidance at all. We bring together the work of many others, and we include rock physics, depth trends, structural information, and uncertainty analysis. It is a workflow that can be adjusted to personal needs and preferences. We choose the Gassmann model to get from velocity to porosity and the self-similar model to get from porosity to resistivity, both as Carcione et al. (2007) present. Following Engelmark (2010), we use the dual-water model from Clavier et al. (1984) to get depth-dependent brine resistivity. Other parameters are either constant or a linear function of depth. Finally, we use Chen and Dickens (2009) to estimate the related uncertainty. The result is a transform that can be applied to seismic velocities to get background resistivities. Once a transform is calibrated, it can be applied to the whole depth extent of seismic velocities without further interaction. Such a background model yields valuable information about the subsurface background resistivity distributions. It can be used for an integrated field analysis and for accurate EM feasibility studies, and it provides a good model to generate synthetic EM responses.

The paper is split into two parts. First, we explain the methodology, namely, the rock-physics models and their depth dependence and the uncertainty analysis; all symbols with their units are listed in Table 2. Second, we apply the theory to data from the North Sea Harding field (Beckly et al., 2003), where a successful EM repeatability experiment was carried out (Ziolkowski et al., 2010). In this repeatability experiment, 1D inversion results were collated to form a 2D resistivity section. However, this result is not very detailed, and it is mainly limited by the chosen layer thicknesses (taken from seismic structures). Furthermore, the 1D inversions resulted in an unrealistically low resistivity contrast with target resistivity of approximately 5 Ωm, embedded in a background with resistivities of approximately 1–3.5 Ωm. To apply the theory, we calibrate our rock-physics model with a well log from Harding South, and we apply it to seismic velocities at Harding Central. A comparison with well data from Harding Central shows that the well-log resistivities fall within the error bounds of our predicted background resistivity model, which validates the accuracy of this approach. This approach yields a resistivity model, including uncertainties, assuming brine in the pore fluids. Any deviation in our EM data from this would be an indicator of the presence of hydrocarbons.

Table 1. Physical properties of geophysical exploration methods (adapted from Ziolkowski and Engelmark, 2009).

Technique and theory	Physical properties	
Gravity	Density	**ϱ**
Newton's law of gravitation		
Laplace's equation		
Seismics	Bulk modulus	**K**
Wave equation (Hooke's law;	Shear modulus	**G**
Newton's laws of mechanics)	Density	**ϱ**
Electromagnetics	Magnetic permeability	**μ**
Maxwell's equations	Electrical resistivity	**ρ**
	Electrical permittivity	**ε**

VELOCITY-TO-RESISTIVITY TRANSFORM

However tempting and desirable it is to analyze seismic data and EM data together, they do not share a common physical property, and hence they cannot be linked by any law of physics. This absence of a physical link is usually overcome with rock physics. Rocks are generally inhomogeneous materials, a mixture of different minerals and pores filled with fluids. Petrophysical mixture theories try to estimate the property of a rock from its individual components, for example, the P-wave velocity of a rock from the P-wave velocities of its minerals and pore fluids. Hence, rock physics models are averages. The simplest ones use arithmetic and harmonic means. (The harmonic mean of v_f and v_s is known as the "time-average" or "Wyllie equation" [Wyllie et al., 1956]).

There are many different rock-physics models to relate velocity to porosity and porosity to resistivity. Some are based on theoretical assumptions, e.g., geometry, such as the self-similar model, the Gassmann equation, or the Hashin-Shtrikman (HS) upper and lower bounds. Others are derived empirically, e.g., Archie or the Raymer equation. The simplest model of a rock is a model with two constituents, one being the minerals of the rock (the solid fraction), and the other being the fluid that occupies the pore space. In this simple case, the volume fraction of the fluid is the porosity of the rock ϕ and the volume fraction of the grains is $1 - \phi$.

A good introduction to mixture theories is given by Berryman (1995), and an overview of velocity-to-resistivity cross-property relations is given by Carcione et al. (2007) (which can be found in Mavko et al., 2009). All petrophysical models assume some knowledge of the subsurface in addition to the P-wave velocities gained

Table 2. Symbols used consistently throughout the paper. Subscripts *f*, *s*, and *m* are used for the fluid fraction, solid fraction, and matrix, respectively (e.g., ρ_f). Superscripts + and – stand for the upper and lower bounds, respectively (e.g., ρ^+).

Symbol	Description	Units
v	P-wave velocity	km/s
ϱ	Density	g/cm^3
K	Bulk modulus	GPa
G	Shear modulus	GPa
ϕ	Porosity	—
ρ	Resistivity	Ωm
ε	Electrical permittivity	F/m
μ	Magnetic permeability	H/m
d	Depth	km
T	Temperature	°C
m	Cementation exponent	—
a	Tortuosity factor	—
κ	Krief exponent	—

from well logs or seismic processing. Additional information may come from well logs, from laboratory measurements on core samples, from the literature, or from experience.

Most relations in the literature include electric conductivity, not resistivity; conductivity is the reciprocal of resistivity. We are searching for resistive rather than conductive bodies in the exploration for hydrocarbons. We therefore express all equations in terms of resistivity. We list in the following sections the models we use later in our example. Any other relation that is mentioned or plotted can be found in Appendix A. Table 2 gives a complete list of variables, together with the applied units. The equations, as presented, assume isotropic, linear, and elastic media.

Velocity to porosity

The P-wave velocity in terms of bulk modulus K, shear modulus G, the densities of the solid and the fluid fraction ϱ_s and ϱ_f, and porosity ϕ is given by

$$v = \sqrt{\frac{K + 4G/3}{(1-\phi)\varrho_s + \phi\varrho_f}}. \tag{1}$$

We use the Gassmann equation to calculate the moduli: Gassmann (1951) derives equations for fluid substitution in porous, elastic media. The Gassmann bulk modulus K_G, as Carcione et al. (2007) give, is

$$K_G = \frac{K_s - K_m + \phi K_m(K_s/K_f - 1)}{1 - \phi - K_m/K_s + \phi K_s/K_f}, \tag{2}$$

where K_s and K_f are the bulk moduli of the solid and the fluid fraction, respectively. Krief's relations (Krief et al., 1990) are used to calculate the dry bulk and shear moduli, K_m and G_m,

$$K_m = K_s(1-\phi)^{\kappa/(1-\phi)}, \tag{3}$$

$$G_m = G_s(1-\phi)^{\kappa/(1-\phi)}, \tag{4}$$

where G_s is the shear modulus of the solid fraction, and Krief et al. (1990) suggest that $\kappa = 3$. We refer to κ as the Krief exponent. The Gassmann equation does not provide a way of calculating porosities directly from velocities. Equation 1 must be solved in an iterative way with K_G and G_m to calculate porosity from P-wave velocity.

Figure 1 shows the velocity-to-porosity transforms for the Gassmann equation, the Raymer equation, the acoustic formation factor (AFF), and the HS bounds for rock parameters as given in Table 3. The porosity range is from 0% to 45%. Note that the Raymer equation, in the form provided, is valid for porosities lower than 37%. All transforms are within the HS bounds, except the AFF for high porosities. It is important to realize that most relations have the realistic assumptions that porosity is 0% if velocity is equals v_s, and it is 100% if velocity is equals v_f.

Porosity to resistivity

The self-similar model from Sen et al. (1981) is based on the self-consistent effective medium theory (Bruggeman, 1935; Hanai, 1960). In this model, the resistivity ρ is given by

$$\rho = \left(\frac{\rho - \rho_s}{\rho_f - \rho_s}\right)^m \rho_f \phi^{-m}, \tag{5}$$

where ρ_s and ρ_f are the resistivities of the solid and the fluid fraction, respectively, ϕ is the porosity, and m is the cementation exponent.

Sen et al. (1981) take the formation fluid as host to derive the relation, which has to be solved iteratively to yield resistivity, whereas a similar model by Bussian (1983) takes the rock as host. For two constituents, the results are the same. (Bussian additionally uses a binomial expansion to provide a direct solution for resistivity, with an approximate criterion for the validity). The self-similar model reduces to the harmonic mean if $m = 1$.

Figure 2 shows porosity-to-resistivity transforms for the self-similar, Archie, and Hermance models, and upper and lower HS bounds. All models are restricted to $\rho_f \le \rho \le \rho_s$; the Archie model would otherwise predict resistivities $\rho \to \infty$ for $\phi \to 0$.

Velocity to resistivity

Figure 3 shows a choice of cross-property relations: the Gassmann equation combined with the self-similar model, the Raymer equation combined with the Hermance model, the Faust equation (with $d = 0.2$ km), and the HS bounds. The bounds were calculated by combining the lower bound from velocity to porosity with the

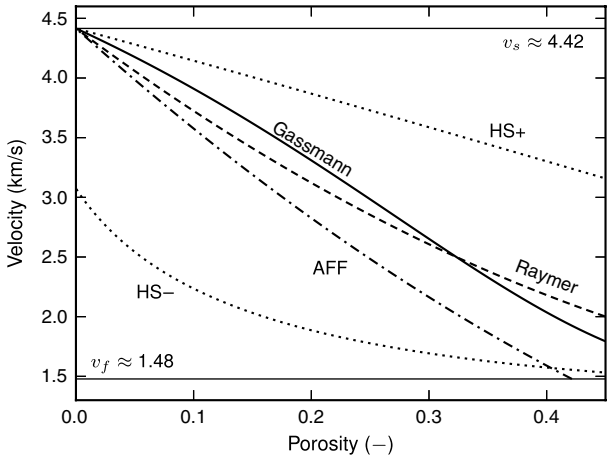

Figure 1. Different velocity-to-porosity transforms for $0 \le \phi \le 0.45$ and $v_f \le v \le v_s$. Note that the AFF for the given parameters falls outside the HS bounds for porosities higher than roughly 40%. The models do not differ significantly. Well data could be fitted by all of these models by calibrating (or adjusting) the rock parameters. The assessment of the uncertainty of a model therefore appears to be more important than the choice of model itself.

Table 3. Material properties used in Figures 1–4; see Table 2 for units (from Carcione et al. [2007], Table 2, shale).

ρ_s	ρ_f	K_s	K_f	G_s	ϱ_s	ϱ_f
5	0.067	25	2.25	20	2.65	1.03

upper bound from porosity to resistivity, and vice versa. The gray area shows where the intermediate porosity is larger than 45% in the Gassmann/self-similar transform. (The area would be similar for the Raymer/Hermance model; there is no intermediate porosity in the Faust equation). The danger in cross-property relations is that one does not see the porosity in the middle, and it is a good idea to limit the possible porosity range; otherwise, the resulting resistivity might look perfectly sensible when, in fact, it is nonsense.

We could have plotted any combination of the previously mentioned transforms. However, we are convinced that the choice of rock physics model does not really matter because they have to be calibrated to every case anyway. One only has to be careful with relations such as Archie, Faust, and AFF. For example, the resistivity tends to infinity as the porosity tends to zero in Archie's equation. The other relations have similar pitfalls for extreme porosities.

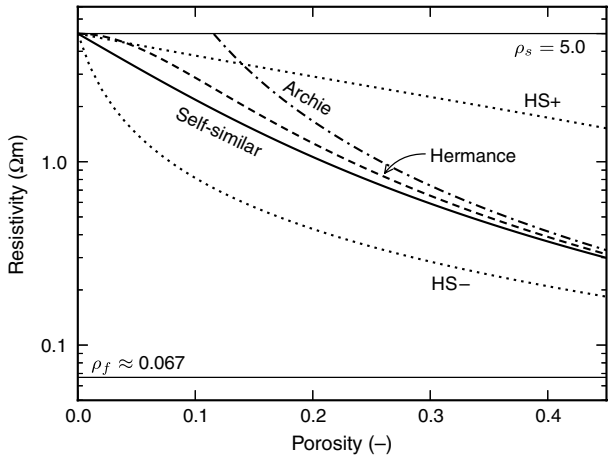

Figure 2. Different porosity-to-resistivity transforms for $0 \le \phi \le 0.45$ and $\rho_f \le \rho \le \rho_s$. These models differ mainly in the low-porosity range. The Archie model is good for porous rocks, but it yields $\rho \to \infty$ for $\phi \to 0$. As in the case for velocity to porosity, the different porosity-to-resistivity models do not differ significantly, and the choice of model is up to personal preference and proper calibration.

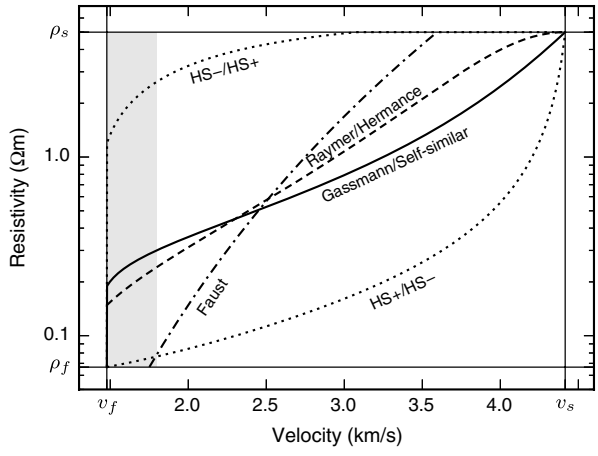

Figure 3. Different velocity-to-resistivity transforms for $v_f \le v \le v_s$ and $\rho_f \le \rho \le \rho_s$. The gray area marks the zone where the intermediate porosity would be greater than 45% in the Gassmann model (as an example). Depth $d = 0.2$ km for Faust.

Depth dependence

A rock-physics model, as established in the previous section, provides a transform from seismic velocity to resistivity. Such a transform is usually calibrated with a set of data, often from well logs, as in our case, or from core samples. However, this transform then holds only for this particular environment. That is because rock properties (like velocity or resistivity) are a function of many parameters, such as pressure, temperature, wetability, residual oil and water saturations, shaliness, porosity, and permeability. We can ignore some of these parameters, such as wetability and residual oil and water saturations, because we are looking for a background model without any hydrocarbons. Others cannot be neglected, for instance, temperature and pressure, which are functions of depth, as a first-order approximation. This depth dependence of the transform is one reason why the Faust equation, an empirically derived relation without a physical foundation, often works very well and is widely used, just like the Archie model in the case of porosity to resistivity.

To get a background resistivity model from seismic data, it is desirable to have a transform that holds for the whole depth range, that is, a transform that can be applied to the seismic velocity cube as a whole. The simplest depth trend would be to calibrate the transform at a shallow and a deep part of the section and establish a linear depth trend. Engelmark (2010) shows that the change of brine resistivity with changing temperature is likely to be the major influence. He successfully applied the dual-water model (Clavier et al., 1984) for the transform from porosity to resistivity. The dual-water model states that there are two kinds of resistivity in the rock: one from the pore water (ionic) and one from the clay-bound water (cation exchange capacity [CEC]). The weight of these two resistivities is a function of the concentration of NaCl and of the CEC. However, Engelmark (2010) obtains good results by using the pore-water resistivity in the shallow, unconsolidated section solely and the clay-bound water resistivity in the deeper, consolidated section solely. He uses the Archie model with the resistivity of sea water for the top 525 m and Archie with the temperature-dependent clay-bound water resistivity from Waxman and Thomas (1974), as given in Dewan (1983, equation 7.22):

$$\rho_f = [6.8(1 + 0.0545T_0 - 1.127 \times 10^{-4}T_0^2)]^{-1}, \quad (6)$$

where $T_0 = T - 25$, ρ_f is the brine resistivity, and T is the temperature in degrees Celsius.

Instead of the resistivity of sea water, we can apply the model of Sen and Goode (1992, equation 9), which provides temperature-dependent pore-water resistivity, incorporating the molality (mol solute per kilogram of solvent) of salt water:

$$\rho_f = \left\{ (5.6 + 0.27T - 1.5 \times 10^{-4}T^2)M - \frac{2.36 + 0.099T}{1.0 + 0.214M} M^{3/2} \right\}^{-1}. \quad (7)$$

Taken as the thermal gradient, this relationship provides basically nothing other than a depth-dependent relation for the resistivity of the pore fluid.

There are other factors that influence a velocity-to-resistivity transform. One of these is resistivity anisotropy, which is known to have a big impact for multitransient EM method (MTEM) modeling (Werthmüller, 2009), but it is neglected in this study. The available well logs commonly measure horizontal conductivity. The procedure presented here therefore provides an estimate of the available horizontal resistivities. If there is an anisotropy estimate from data, modeling, or experience, it can be incorporated into the final model. In any case, a slight resistivity anisotropy of $\lambda \approx 1.5$ might be more realistic than the isotropic assumption (where λ is the square root of the ratio of vertical over horizontal resistivity $\lambda = \sqrt{\rho_v/\rho_h}$). Overpressure affects velocity and resistivity differently, as can be seen in Eaton's pore pressure equations (Eaton, 1975). It is another factor that could improve a velocity-to-resistivity transform and that could be implemented in the framework presented here.

Structural information

Seismic data provide more information than just seismic velocities. They are particularly good at detecting elastic and acoustic impedance contrasts, which delineate geologic structures in 3D. In addition to depth constraints, a velocity-to-resistivity transform can be improved by using different transforms for different lithologies, e.g., one model for shaley sections and another model for sandstone sections.

UNCERTAINTY

There exist many different rock-physics models to link seismic velocity to electric resistivity, as we have seen. Some of them use an intermediate variable, mostly porosity; others are a direct function. Whatever the choice of the rock-physics model, we gain a resistivity value derived from rock physics ρ_{rp}, which is a function of seismic P-wave velocity v and other parameters,

$$\rho_{rp} = f(v, \theta), \tag{8}$$

where the other parameters are here summarized by θ. In our example, we use the relations given in equations 1–5; hence, we have relations in the form of

$$\rho_{rp} = f_s(\rho_s, \rho_f, m, \phi), \tag{9}$$

where

$$\phi = f_G(K_s, K_f, G_s, \varrho_s, \varrho_f, \kappa, v). \tag{10}$$

Here, f_s stands for the self-similar model and f_G for the Gassmann-based relations.

Using rock-physics modeling to get resistivities from seismic velocities introduces two kind of errors. The parameters in the model (ρ_s, ρ_f, m, K_s, K_f, G_s, ϱ_s, ϱ_f, κ, v) have errors, and the models (f_s, f_G) themselves have errors. These errors are likely to be bigger than the errors in the data themselves, as Myoung and Snieder (2011) show. We adapt the methodology of Chen and Dickens (2009), who emphasize that parameter uncertainty and model uncertainty have to be taken into account.

They describe the rock physics model as a gamma distribution with error E:

$$f(\rho|v, \theta) = \frac{\beta^\alpha \rho^{\alpha-1}}{\Gamma(\alpha)} \exp(-\beta\rho), \tag{11}$$

where θ is a vector containing all model parameters, the shape parameter $\alpha = 1/E^2$, and the scale parameter $\beta = (\alpha - 1)/\rho_{rp}$. The parameters themselves are described as uniform distributions of a defined error around our best estimate. To get the probability density function (PDF) of the whole range of possible parameters, one has to integrate over all values,

$$f(\rho|v) = \int f(\rho|v, \theta) f(\theta|v) \mathrm{d}\theta. \tag{12}$$

We use a Markov chain Monte Carlo (MCMC) sampler to calculate the distribution, as Chen and Dickens (2009) suggest (for more details, see Appendix B). The result of this methodology is resistivity ρ as a PDF for any given set of model parameters, instead of a single deterministic value ρ_{rp}, as shown in Figure 4. The gray line shows the deterministic resistivity value resulting from the Gassmann/self-similar equation with the parameters given in Table 3 and velocity $v = 2.5$ km/s. The dashed curve shows the distribution if the model has no uncertainty, but with the parameters uniformly distributed with a range of ±5%. The dashed-dotted curve shows the distribution if the parameters have no error, but the rock physics model is a gamma distribution with $E = 0.05$. And finally, the solid curve shows the distribution if both uncertainties are taken into account. The parameter uncertainty is more important than the model uncertainty in this example. However, both contribute to the final PDF, and their relative contributions vary from case to case.

Even though a seismic section never displays an error bar, seismic data have errors too. To quantify the error in seismic data is difficult, and one would have to take into account acquisition and processing errors. In Figure 4, we assigned to the seismic velocities the same error as to all the other parameters. However, with the real data, we estimate the uncertainty in seismic velocities from the data themselves, using the same well logs we use to calibrate our rock-physics model, which we show in the example section.

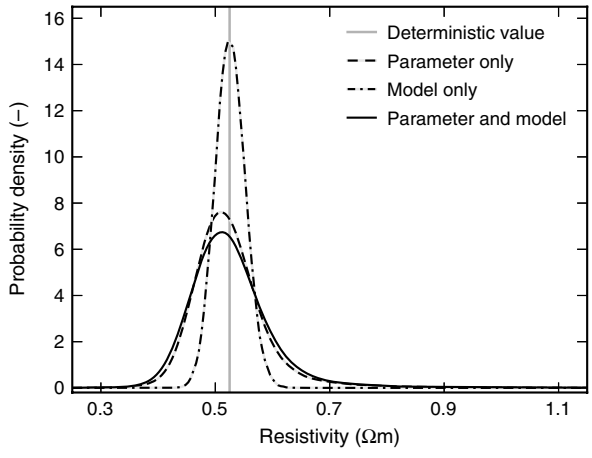

Figure 4. Example of the uncertainty analysis applied to the Gassmann/self-similar transform for velocity $v = 2.5$ km/s and the parameters in Table 3. The applied error is 5% for the uncertainty of each parameter and of the model.

EXAMPLE: THE HARDING FIELD

Our study area is the North Sea Harding field, operated by BP and Maersk. The field is a medium-size oil and gas field at a depth of about 1.7 km; the water depth is approximately 110 m. See Beckly et al. (2003) for a thorough description. Two CSEM surveys with a transient source signal were carried out in 2007 and 2008 in a successful EM repeatability experiment described by Ziolkowski et al. (2010). MTEM is described in Ziolkowski et al. (2007). The source dipole current signal in MTEM is a measured pseudo-random binary sequence, which allows the impulse responses of the subsurface to be recovered from the measured receiver responses. The full spectrum of the earth response is recovered. Figure 5 shows the outline of Harding Central and Harding South, the location of the wells used, and the EM acquisition line, which passes the discovery well 9/23b-7 and the dry well 9/23a-3. In this repeatability experiment, 1D inversion results were collated to form a 2D resistivity section, where the layer thicknesses were derived from the seismic data. The result is mainly constrained by these chosen layers. The resulting 1D models fit the EM data reasonably well; however, we do not know if they are realistic or not, due to the nonuniqueness of, specifically, 1D EM inversion.

First, we calibrate our rock-physics model with well 9/23b-8 from Harding South. Second, we check this transform with the other well logs. Third, satisfied by this control, we apply this transform to a seismic velocity section along the EM line to get a detailed model of the background resistivities. The result is a 2D background resistivity model. However, we can also apply the same transform to the whole seismic cube, to get a 3D background resistivity model of our area of interest. We do not do this here because it does not add anything to the methodology described.

Figure 6 shows P-wave velocity versus resistivity from well 9/23b-8 for relatively clean shale sections, color-coded for different depth intervals. The depth trend is clearly visible, with resistivities becoming smaller and velocities higher for deeper sections. The data indicate a weak relationship between velocity and resistivity. This relation is what we try to capture with the rock-physics transform from velocity to resistivity, incorporating the noticeable depth trend.

Seismic velocity uncertainty

We assign our rock-physics model and all involved parameter errors as described in the first part of the paper: The Gassmann/self-similar transform is described as a gamma distribution with an error of 5%, and the parameters are uniformly distributed around our best estimate with an error of ±5%. Exceptions to this are the seismic velocities. Seismic sections and seismic velocities usually come without a measure of the associated error. Errors in seismic velocities come from acquisition and processing. However, it is not an easy task to estimate this error. We use the well log data to get an estimate of the variability of seismic velocities. Figure 7a shows the velocity measurements of well 9/23b-8, where the gray curve (v) is the original data and the black curve (v^s) is the original data smoothed using a Hanning window over 320 samples (≈48.8 m). The smoothed curve reflects the expected resolution of CSEM data better than the 15-cm (6-in) sampling of the well log. We now define our velocity distribution as the difference between the log values and the values of the smoothed log, $v(z) - v^s(z)$. This method is a good measure for the variability of velocities, and the resulting distribution is thought to be wider than errors in seismic velocities resulting from acquisition and processing of seismic data. The resulting distribution is shown in Figure 7b, where the PDF of this data distribution is found with a Gaussian kernel density estimation. This approach should be replaced with a better estimate of seismic velocity uncertainty, if it is available. The point is to estimate velocity uncertainty from the data.

Calibration and depth trend

Figure 8a and 8b shows the original (gray) and smoothed (black) velocity and resistivity logs of our calibration well 9/23b-8 and the mode and ±1 and ±2 standard deviations of our analysis in red, cyan, and magenta, respectively. We wanted the transform to be as simple as possible, yet be able to predict the whole depth range.

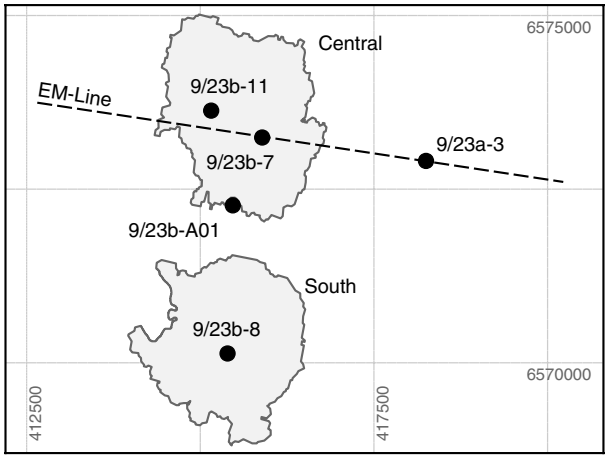

Figure 5. Location of Harding Central and Harding South, the EM survey outlines from 2007 and 2008, and the five wells we use in our example. Well 9/23b-8 is our calibration well. Wells 9/23b-7, 9/23b-11, 9/23b-A01, and 9/23a-3 are our control wells, where the ultimate one is off-target.

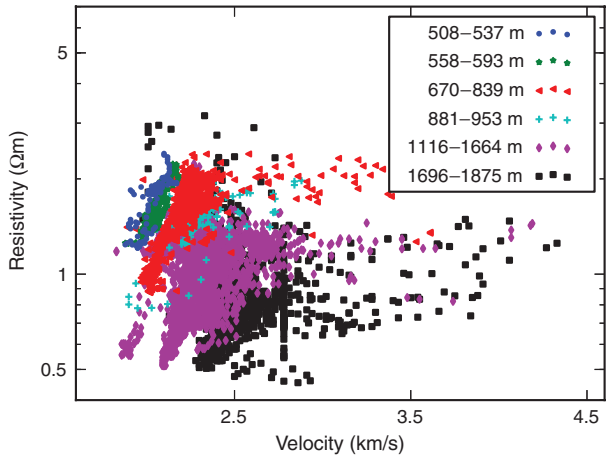

Figure 6. Velocity versus resistivity plot for some relatively clean shale sections in well 9/23b-8. There seems to be a weak relationship between velocity and resistivity, which rock physics tries to predict. Note the depth trend; resistivity is generally decreasing and velocity is increasing with increasing depth.

One of the difficulties with rock-physics transforms is that they usually hold for only a very specific environment, for instance, for a specific depth range. The seismic velocities in Harding are between 1.5 and 3 km/s in the shallow part, but up to 6 km/s in the deeper part. We therefore model the bulk and shear moduli of the solid fraction as linear functions of depth to allow velocities to increase with increasing depth: The bulk modulus is defined as $K_s = 10 + 15d$ GPa, and the shear modulus is defined as $G_s = 5 + 13d$ GPa; d is depth in kilometers. Fixed parameters are the density of the solid fraction $\varrho_s = 2.65$ g/cm^3, the density of the fluid fraction $\varrho_f = 1.03$ g/cm^3, and the bulk modulus of the fluid fraction $K_f = 2.25$ GPa. Following Engelmark (2010), we make the cementation exponent a function of porosity $m = 2.1 - \phi$, and we furthermore define the Krief exponent as a function of depth $\kappa = 3.2 - 0.4d$. The resistivity of the solid fraction is given by $\rho_s = 3 + 10d$ Ωm. The sum of the free-water resistivity, equation 6, and the bound-water resistivity, equation 7, yields in our case the best result for the fluid resistivity. However, equation 6 yields unreasonable values for shallow depths (hence low temperatures). We therefore apply it from 350 m below the mudline downward, and we keep it constant above.

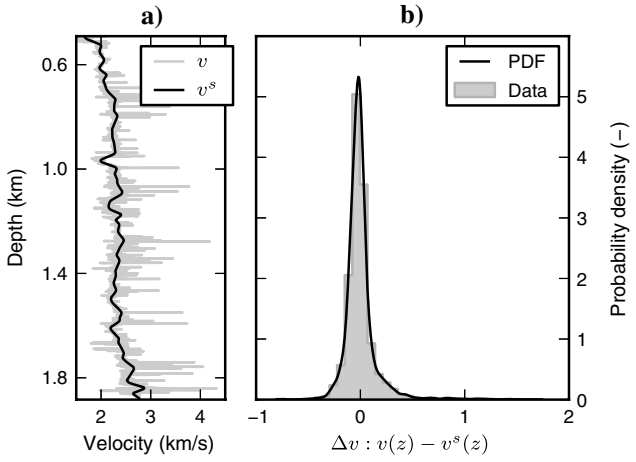

Figure 7. Velocity log of well 9/23b-8. The gray curve (v) is the original log, and the black curve (v^s) is smoothed with a Hanning window over 320 samples. We estimate the P-wave velocity distribution from the well log data by taking the difference of the original and the smoothed data $v(z) - v^s(z)$.

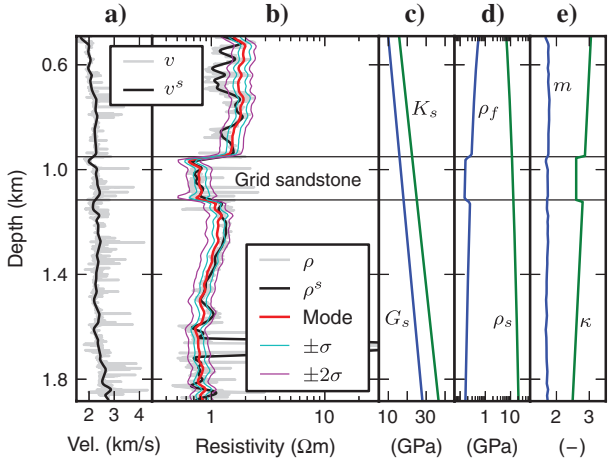

Figure 8. (a) Velocity and (b) resistivity log of well 9/23b-8. The gray curve is the original log, and the black curve is smoothed with a Hanning window over 320 samples. The red curve is the mode of the PDFs from the uncertainty analysis using the Gassmann/self-similar velocity-to-resistivity relation. The cyan and magenta curves are $\pm\sigma$ and $\pm 2\sigma$, respectively. Plots (c, d, e) show all depth-dependent parameters: $K_s, G_s, \rho_s, \rho_f, m$, and κ.

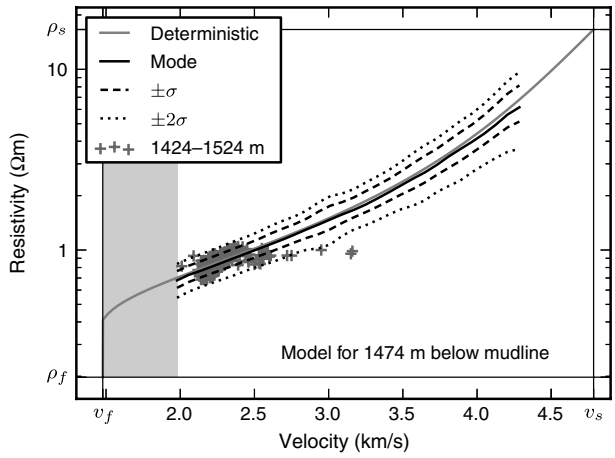

Figure 9. Comparison of the rock physics model and uncertainty analysis with well data. The plotted well data are from within 1424–1524-m depth of well 9/23b-8. The depth is set to $z = 1.474$ km for the depth-dependent parameters. The deterministic result of the transform is shown in gray, and the outcome of the uncertainty analysis is shown in black. The well data are within $\pm 2\sigma$, except for some high-velocity outliers originating from thin limestone layers.

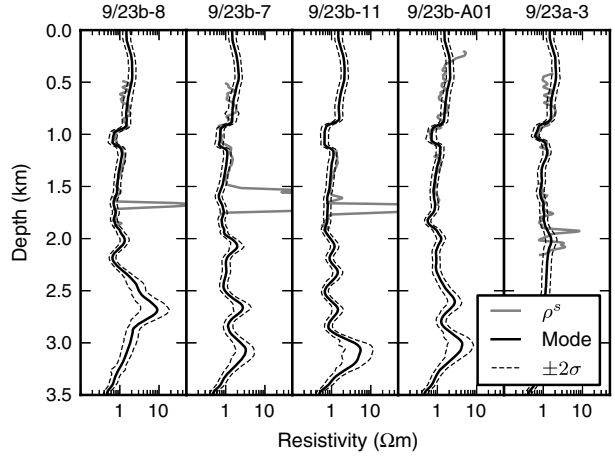

Figure 10. Well logs (gray) and the mode (black) and $\pm 2\sigma$ (dashed) of the resistivity predictions calculated using the seismic velocities. Well 9/23b-8 (leftmost) is the calibration well. The same transform applied to four wells on Harding Central shows a good match: Most well measurements lie within $\pm 2\sigma$. High resistive, hydrocarbon-bearing formations are not predicted because we assume brine-filled pores. Shallow, sandy sections are also poorly resolved, except for the Grid sandstones, which we explicitly incorporated into our model.

We include an example of structural constraints in the form of the Grid sandstones, which are outlined from picked horizons in the seismic data. The same parameters are used for the Grid sandstones, except that $\kappa = 2.6$, and the fluid resistivity is given by the free water resistivity solely because sands have no clay-bound water. Figure 8c–8e shows all the depth-dependent values. This rock-physics transform is able to predict the resistivities for the whole depth range of the well log. However, the predictions are a bit too high for some shallow, sandy sections. These sand sections could be handled in the same way as we treat the Grid sandstones.

Figure 9 shows a depth snapshot of the calibration of the transformation for $z = 1.474$ km, together with the well data of $z \pm 50$ m. With the exception of some high-velocity values, resulting mostly from thin limestone layers, the mode of the uncertainty analysis $\pm 2\sigma$ includes all the well samples.

Near-field scenario

We now use this calibration from Harding South and test it on a field nearby, Harding Central. We apply the rock-physics transform with the same parameters described before to the Harding Central velocity cube, and we compare them first with well logs. Figure 10 shows the well logs and the mode as well as $\pm 2\sigma$ of the resistivity calculated from the seismic velocities. The predicted resistivities match the well logs very accurately, except for the hydrocarbon-bearing formations. This is exactly what we want because we are interested in a background resistivity model.

The result of our velocity-to-resistivity transform is shown in Figure 11. Figure 11a shows the mode of our resistivity distributions, derived from the seismic velocities shown in Figure 11b. It is a slice through the velocity cube along the EM line from 2007 and 2008, including some major horizons, such as the Grid sandstones and the Balder formation, well 9/23b-7, and the start and end points of these surveys. Figure 11c and 11d shows the mode $\pm$ one standard deviation of the resistivity distributions. Applying the transform to the velocity cube instead of just a slice yields a 3D resistivity background model. Please note one limitation: The transform is calibrated using well-log measurements from a vertical well, which measure mainly horizontal resistivity. These models therefore provide an estimate of horizontal resistivities. Reasonable

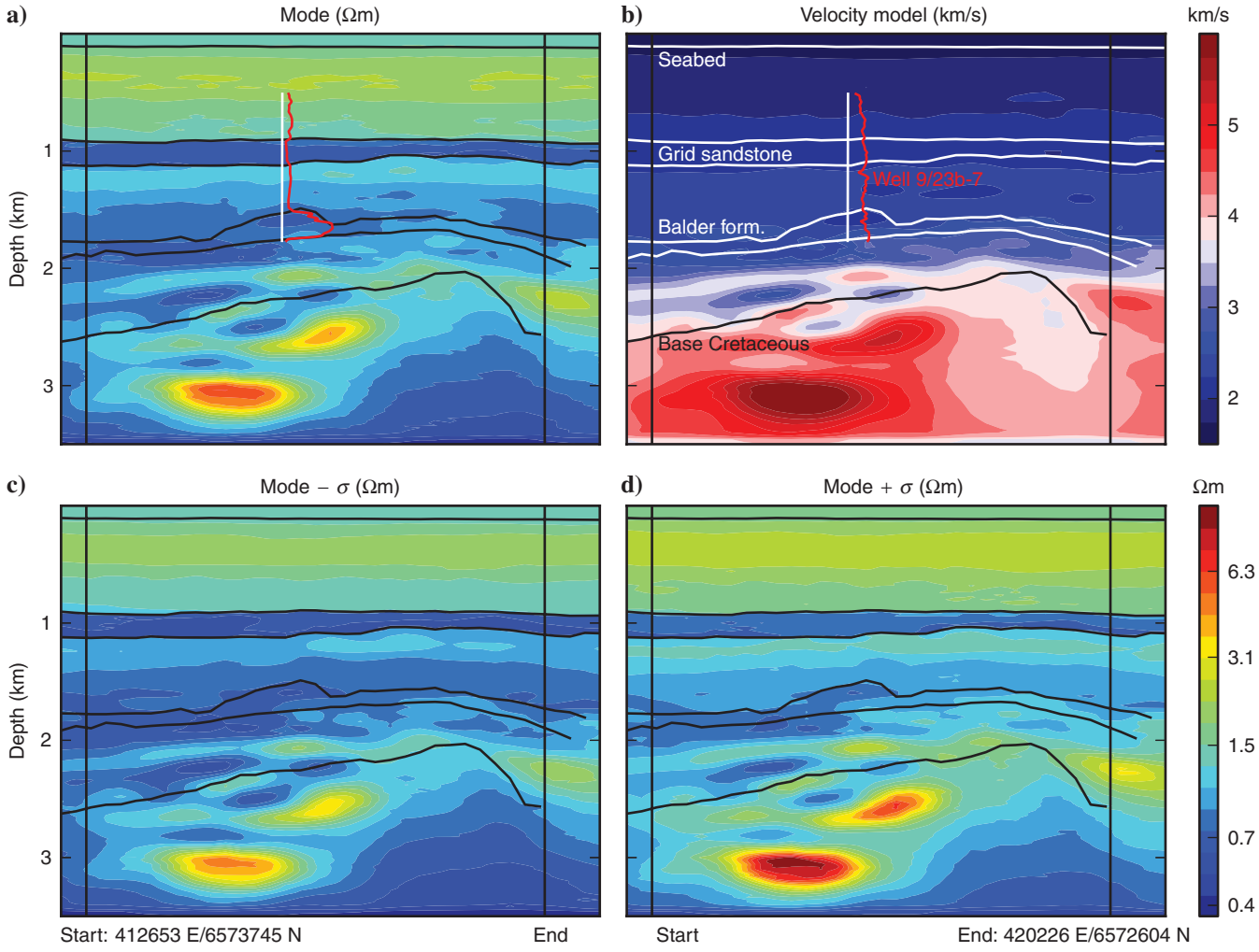

Figure 11. (a) The mode of our background resistivity model, derived from the velocity model in (b); well 9/23b-7 and some major formations are annotated. (c, d) The mode with $-\sigma$ and $+\sigma$, respectively. These resistivities represent horizontal resistivities because they are calibrated with a vertical well log, which mainly measures horizontal resistivities.

anisotropy values have to be estimated independently of the approach presented here.

CONCLUSIONS

We present a methodology to estimate the range of background resistivity models that is consistent with known seismic velocities. We apply and extend known methods. The approach uses depth-dependent petrophysical cross-property relations and uncertainty analysis of the data and the model. Our near-field exploration example shows that this methodology yields a good estimate of background resistivities away from our control point, and hence it provides an excellent additional data set, which can be used for integrated analysis or as a starting point for a detailed CSEM feasibility study or (iterative) forward modeling. Using a probability distribution instead of fixed values for the background model decreases the influence of unwanted bias that originates from the different physical properties of the seismic and EM methods. Additionally, the uncertainty estimates yield error bars to this data set and the PDFs can be incorporated into weighting functions for 3D inversion schemes, in which the background resistivities would be limited to these values.

This workflow needs fine tuning from case to case because it is not always easy to find a single rock-physics model that fits a large depth range. Every part of the scheme is disputable, and other models might fit better in other cases; it is also a function of personal experience and preference. The Gassmann and the self-similar model are two choices out of many, as is the gamma distribution for the model uncertainty. The more that is known of the present rock-physics parameters, the better are the estimates of their uncertainties. An individual uncertainty for each parameter might therefore be more sensible than our approach of assigning a range of 5% to each of them. Similar conclusions apply to the depth trend, where we could choose many more horizons and include different rock physics models for different lithologies in general. However, our approach was to be as simple as possible, yet as complex as necessary. The resulting background resistivity model is, in any case, a much better resistivity model than a uniform half-space (often used as a starting model in inversion), and it is corroborated by the good match with the well logs. We have shown only a slice along the EM line. However, we can apply the transform to the entire velocity cube. This gives us the range of possible 3D background resistivity models of the whole area.

Having well-log information for calibration is crucial. Our example shows that this well log does not necessarily have to be from the field of interest, but it should be from within the region of interest. The calibration issue remains a problem above and below the depths of available logs, where other information might help to improve the calibration. Furthermore, the calibration with well logs also limits us to predict horizontal resistivities. Reasonable anisotropy values have to be found independently of this approach.

ACKNOWLEDGMENTS

We thank PGS for funding the research and the Harding partners, BP and Maersk, for permission to show the data. We appreciate valuable comments on rock physics from F. Engelmark (PGS) and on the Harding field from R. Parr (BP) and the continuous support of the whole PGS EM team. We thank the assistant editor, J. Carcione, the associate editor, M. Everett, and two anonymous reviewers, whose feedback greatly improved the clarity of the manuscript.

APPENDIX A

ADDITIONAL ROCK-PHYSICS EQUATIONS

The following is a short description of rock physics models that have been used in figures or mentioned in the main text but have not been used in our real example nor explained in detail. To get from velocity to resistivity, we are interested in porosity as a function of velocity $\phi(v)$ and resistivity as a function of porosity $\rho(\phi)$. We provide velocity as a function of porosity, too, $v(\phi)$ because this shows more clearly how the average was derived, and hence it often helps to understand the relationship. Furthermore, it is the way the relations are usually presented. All symbols and their units are declared in Table 2 if not specifically given here.

Porosity from velocity

The Raymer equations are a set of empirical relations for different ranges of porosity, given by Raymer et al. (1980). The relation for porosities $\phi < 37\%$ is given by

$$\phi = \frac{-\sqrt{4v_s(v - v_f) + v_f^2} + 2v_s - v_f}{2v_s},$$
$$v = (1-\phi)^2 v_s + \phi v_f. \tag{A-1}$$

The AFF is a simpler version of the Raymer equation given in equation A-1, neglecting the velocity of the fluid fraction:

$$\phi = 1 - \left(\frac{v}{v_s}\right)^{1/m}, \qquad v = (1-\phi)^m v_s, \tag{A-2}$$

where m is the cementation exponent, again similar to the Archie model.

The HS Bounds provide a measure of the bulk and shear moduli without specifying the shape of the grains. Hashin and Shtrikman (1963) derive their bounds from mixture models of the elastic moduli, rather than of the velocities. These bounds define the upper and lower bounds of the physically possible values of these moduli, and hence of velocity. Following Berryman (1995) for the two constituents yields

$$K^- = \left(\frac{\phi}{K_f} + \frac{1-\phi}{K_s}\right)^{-1}, \tag{A-3}$$

$$K^+ = \left(\frac{1-\phi}{K_s + \frac{4}{3}G_s} + \frac{\phi}{K_f + \frac{4}{3}G_s}\right)^{-1} - \frac{4}{3}G_s \tag{A-4}$$

for the bulk moduli and

$$G^- = 0, \tag{A-5}$$

$$G^+ = \left(\frac{1-\phi}{G_s + \eta} + \frac{\phi}{\eta}\right)^{-1} - \eta, \qquad \eta = \frac{G_s}{6}\left(\frac{9K_s + 8G_s}{K_s + 2G_s}\right) \tag{A-6}$$

for the shear moduli. The HS bounds yield, together with equation 1, the porosity for a given P-wave velocity in an iterative manner.

Resistivity from porosity

Archie's law is an empirical relationship given by

$$\rho = a\rho_f \phi^{-m}, \tag{A-7}$$

where m is the cementation exponent and a is the tortuosity factor. Archie (1942) finds this relationship empirically by analyzing resistivity measurements in the laboratory. He examines clean reservoir sandstones, and Archie's law hence holds for shale-free, porous sandstones, where m is close to two and a is one. The tortuosity factor is often used to make Archie's law work for shaley sandstones.

The Hermance model is an adaptation of Archie's law. It takes the resistivity of the grains into account with the harmonic mean:

$$\rho = \left(\frac{\phi^m}{\rho_f} + \frac{1-\phi^m}{\rho_s}\right)^{-1}. \tag{A-8}$$

The only difference between Hermance (1979) and the harmonic mean is the cementation exponent m, which weights the solid fraction higher than the fluid fraction. (Note that the harmonic mean of resistivities equals the arithmetic mean of conductivities).

The HS bounds provide upper and lower limits if the geometry is not specified (Hashin and Shtrikman, 1963). For the case of two constituents, they are given by Berryman (1995)

$$\rho^- = \left[\left(\frac{(1-\phi)\rho_f\rho_s}{\rho_f + 2\rho_s} + \frac{\phi\rho_f}{3}\right)^{-1} - \frac{2}{\rho_f}\right]^{-1}, \tag{A-9}$$

$$\rho^+ = \left[\left(\frac{(1-\phi)\rho_s}{3} + \frac{\phi\rho_f\rho_s}{2\rho_f + \rho_s}\right)^{-1} - \frac{2}{\rho_s}\right]^{-1}. \tag{A-10}$$

These bounds are true if $\rho_f < \rho_s$, which is generally the case if we have conductive brines in the pores. The bounds are reversed if $\rho_s < \rho_f$, and the upper bound becomes the lower, and vice versa.

Resistivity directly from velocity

The Faust equation is an oft-cited model that calculates resistivity directly from velocity, without porosity as the connecting parameter, but with a depth dependence (Faust, 1953):

$$\rho = \frac{\rho_f}{d}\left(\frac{v}{2.289}\right)^6, \tag{A-11}$$

where d is the depth in kilometers. The reasons it is often used and often works fairly well are first, its simplicity and second, the depth trend.

APPENDIX B

PyMC

The uncertainty analysis was calculated using the PyMC module in Python; see Patil et al. (2010). PyMC is an open-source project under an Academic Free License with almost 10 years of development; the aim of the authors is to make MCMC "more accessible to nonstatisticians." The source code can be found on github, https://github.com/pymc-devs/pymc, along with extensive documentation, in addition to the afore-referenced paper. We calculated 50,000 samples without burn-in and a thinning factor of 25 because the sampler could get stuck in the low-probability tails of the V_P distribution from the well log. The PDFs shown were then estimated with a Gaussian kernel density estimation.

REFERENCES

Archie, G. E., 1942, The electrical resistivity log as an aid in determining some reservoir characteristics: Transactions of the AIME, 54–62, doi: 10.2118/942054-G.

Beckly, A. J., T. Nash, R. Pollard, C. Bruce, P. Freeman, and G. Page, 2003, The Harding Field, block 9/23b, *in* J. G. Gluyas, and H. M. Hichens, eds., United Kingdom oil and gas fields commemorative millennium volume: The Geological Society of London, Geological Society Memoir 20, 283–290.

Berryman, J. G., 1995, Mixture theory for rock properties, *in* T. J. Ahrens, ed., Rock physics & phase relations: A handbook of physical constants: AGU, **3**, 205–228.

Bruggeman, D. A. G., 1935, Berechnung verschiedener physikalischer Konstanten von heterogenen Substanzen. I: Dielektrizitätskonstanten und Leitfähigkeiten der Mischkörper aus isotropen Substanzen: Annalen der Physik, **416**, 636–664, doi: 10.1002/andp.19354160705.

Bussian, A. E., 1983, Electrical conductance in a porous medium: Geophysics, **48**, 1258–1268, doi: 10.1190/1.1441549.

Carcione, J. M., B. Ursin, and J. I. Nordskag, 2007, Cross-property relations between electrical conductivity and the seismic velocity of rocks: Geophysics, **72**, no. 5, E193–E204, doi: 10.1190/1.2762224.

Chen, J., and T. A. Dickens, 2009, Effects of uncertainty in rock-physics models on reservoir parameter estimation using seismic amplitude variation with angle and controlled-source electromagnetics data: Geophysical Prospecting, **57**, 61–74, doi: 10.1111/j.1365-2478.2008.00721.x.

Clavier, C., G. Coates, and J. Dumanoir, 1984, Theoretical and experimental bases for the dual-water model for interpretation of shaly sands: Journal of Petroleum Technology, **24**, 153–168, doi: 10.2118/6859-PA.

Constable, S., and L. J. Srnka, 2007, An introduction to marine controlled-source electromagnetic methods for hydrocarbon exploration: Geophysics, **72**, no. 2, WA3–WA12, doi: 10.1190/1.2432483.

Constable, S. C., R. L. Parker, and C. G. Constable, 1987, Occam's inversion: A practical algorithm for generating smooth models from electromagnetic sounding data: Geophysics, **52**, 289–300, doi: 10.1190/1.1442303.

Dewan, J. T., 1983, Essentials of modern open-hole log interpretation: Pennwell Corp.

Eaton, B. A., 1975, The equation for geopressure prediction from well logs: Society of Petroleum Engineers of AIME Technical Program, Expanded Abstracts, 5544-MS.

Engelmark, F., 2010, Velocity to resistivity transform via porosity: 80th Annual International Meeting, SEG, Expanded Abstracts, 2501–2505.

Faust, L. Y., 1953, A velocity function including lithologic variation: Geophysics, **18**, 271–288, doi: 10.1190/1.1437869.

Gallardo, L. A., and M. A. Meju, 2007, Joint two-dimensional cross-gradient imaging of magnetotelluric and seismic traveltime data for structural and lithological classification: Geophysical Journal International, **169**, 1261–1272, doi: 10.1111/j.1365-246X.2007.03366.x.

Gassmann, F., 1951, Über die Elastizität poröser Medien: Vierteljahrsschrift der Naturforschenden Gesellschaft in Zürich, **96**, 1–23.

Hanai, T., 1960, Theory of the dielectric dispersion due to the interfacial polarization and its application to emulsions: Colloid & Polymer Science, **171**, 23–31, doi: 10.1007/BF01520320.

Harris, P., Z. Du, L. MacGregor, W. Olsen, R. Shu, and R. Cooper, 2009, Joint interpretation of seismic and CSEM data using well log constraints: An example from the Luva Field: First Break, **27**, 73–81.

Hashin, Z., and S. Shtrikman, 1963, A variational approach to the theory of the elastic behaviour of multiphase materials: Journal of the Mechanics and Physics of Solids, **11**, 127–140, doi: 10.1016/0022-5096(63)90060-7.

Hermance, J. F., 1979, The electrical conductivity of materials containing partial melt: A simple model from Archie's law: Geophysical Research Letters, **6**, 613–616, doi: 10.1029/GL006i007p00613.

Hu, W., A. Abubakar, and T. M. Habashy, 2009, Joint electromagnetic and seismic inversion using structural constraints: Geophysics, **74**, no. 6, R99–R109, doi: 10.1190/1.3246586.

Krief, M., J. Garat, J. Stellingwerff, and J. Ventre, 1990, A petrophysical interpretation using the velocities of P and S waves (full-waveform sonic): The Log Analyst, **31**, 355–369.
Mavko, G., T. Mukerji, and J. Dvorkin, 2009, The rock physics handbook: Cambridge University Press.
Myoung, J. K., and R. Snieder, 2011, Uncertainty analysis for the integration of seismic and controlled source electro-magnetic data: Geophysical Prospecting, **59**, 609–626, doi: 10.1111/j.1365-2478.2010.00937.x.
Patil, A., D. Huard, and C. J. Fonnesbeck, 2010, PyMC: Bayesian stochastic modelling in Python: Journal of Statistical Software, **35**, 1–81.
Raymer, L. L., E. R. Hunt, and J. S. Gardner, 1980, An improved sonic transit time-to-porosity transform: Presented at SPWLA 21st Annual Logging Symposium.
Sen, P. N., and P. A. Goode, 1992, Influence of temperature on electrical conductivity on shaly sands: Geophysics, **57**, 89–96, doi: 10.1190/1.1443191.
Sen, P. N., C. Scala, and M. H. Cohen, 1981, A self-similar model for sedimentary-rocks with application to the dielectric constant of fused glass-beads: Geophysics, **46**, 781–795, doi: 10.1190/1.1441215.
Waxman, M. H., and E. C. Thomas, 1974, Electrical conductivities in shaly sands — I: The relation between hydrocarbon saturation and resistivity index; II: The temperature coefficient of electrical conductivity: Journal of Petroleum Technology, **26**, 213–225, doi: 10.2118/4094-PA.
Werthmüller, D., 2009, Inversion of multi-transient EM data from anisotropic media: Master's thesis, TU Delft.
Wyllie, M. R. J., A. R. Gregory, and L. W. Gardner, 1956, Elastic wave velocities in heterogeneous and porous media: Geophysics, **21**, 41–70, doi: 10.1190/1.1438217.
Ziolkowski, A., and F. Engelmark, 2009, Use of seismic and EM data for exploration, appraisal and reservoir characterization: CSPG CSEG SWLS Joint Convention, Expanded Abstracts, 424–427.
Ziolkowski, A., B. Hobbs, and D. Wright, 2007, Multitransient electromagnetic demonstration survey in France: Geophysics, **72**, no. 4, F197–F209, doi: 10.1190/1.2735802.
Ziolkowski, A., R. Parr, D. Wright, V. Nockles, C. Limond, E. Morris, and J. Linfoot, 2010, Multi-transient electromagnetic repeatability experiment over the North Sea Harding field: Geophysical Prospecting, **58**, 1159–1176, doi: 10.1111/j.1365-2478.2010.00882.x.
Ziolkowski, A., and D. Wright, 2012, The potential of the controlled source electromagnetic method: A powerful tool for hydrocarbon exploration, appraisal, and reservoir characterization: IEEE Signal Processing Magazine, **29**, no. 4, 36–52, doi: 10.1109/MSP.2012.2192529.